Modeling the improved hydrogen embrittlement tolerance of twin boundaries in face-centered cubic complex concentrated alloys

Anne Marie Z. Tan[a,b,*], Zhi Li[a], Yakai Zhao[c], Upadrasta Ramamurty[b,c], Huajian Gao[b,a,1]

[a] *Institute of High Performance Computing (IHPC), Agency for Science, Technology and Research (A*STAR), 1 Fusionopolis Way, #16-16 Connexis, Singapore 138632, Singapore*
[b] *School of Mechanical and Aerospace Engineering, Nanyang Technological University, Singapore 639798, Singapore*
[c] *Institute of Materials Research and Engineering (IMRE), Agency for Science, Technology and Research (A*STAR), 2 Fusionopolis Way, Innovis #08-03, Singapore 138634, Singapore*

Abstract

With increasing interest in hydrogen as an alternative fuel, there is a need to develop structural alloys with improved resistance to hydrogen embrittlement (HE) for application in the new hydrogen economy. Complex concentrated alloys (CCAs), which include high entropy alloys and their derivatives, medium entropy alloys, are a new class of structural materials, some of which have reported improved HE resistance. While some studies have suggested that the improved HE resistance in CCAs with the face-centered cubic (fcc) crystal structure may be due to the high density of nanotwins within them, a detailed mechanistic understanding is yet to be developed. Towards that end, following the approach of Zhou, Tehranchi and Curtin, we employ a density functional theory-informed Griffith-Rice model[2] to predict the ductile or brittle response of a crack tip interacting with twin boundaries (TBs) in a model fcc CCA, CrCoNi, both in the absence of and presence of hydrogen. Both the model and molecular dynamics simulations predict that TBs in fcc alloys are not inherently more susceptible to HE than the bulk matrix, and could in fact improve HE resistance by retarding cracks while promoting dislocation emission along the TB. Thus, designing fcc CCAs with a high density of nanotwins or utilizing gradient nanotwinned structures

*Corresponding author
Email addresses: anne_marie_tan_zhao_hui@ihpc.a-star.edu.sg (Anne Marie Z. Tan), li_zhi@ihpc.a-star.edu.sg (Zhi Li), Zhao_Yakai@imre.a-star.edu.sg (Yakai Zhao), uram@ntu.edu.sg (Upadrasta Ramamurty), gao.huajian@tsinghua.edu.cn (Huajian Gao)
[1] Present address: Center for Advanced Mechanics and Materials, Applied Mechanics Laboratory, Department of Engineering Mechanics, Tsinghua University, 100084 Beijing, China
[2] This type of model has also been referred to in the literature as the Rice-Thomson model. In this work, we refer to it as the Griffith-Rice model to reflect that the concept of unstable stacking fault energy was introduced into the model due to Rice (1992) [1].

could be a way forward for realizing alloys with high HE resistance.

Keywords: hydrogen embrittlement, complex concentrated alloys, twin boundary, fracture

1. Introduction

Hydrogen embrittlement (HE), which refers to the deterioration in the mechanical properties of metals and alloys due to the presence of absorbed hydrogen, was first observed almost 150 years ago in steels [2]. Since then, HE has also been observed in many other metals and alloys, including nickel-, cobalt- and iron-based superalloys [3, 4, 5, 6, 7]. Hydrogen embrittlement can severely reduce the ductility and toughness of a material, causing the component to fail in a brittle manner, posing major safety concerns. In recent years, with increasing interest in hydrogen as an alternative fuel, there is an ever more pressing need to understand the underlying mechanisms of HE, and to develop new structural alloys with improved HE resistance.

Mechanistically, hydrogen embrittlement is highly complex and numerous mechanisms have been proposed to explain it. Some of the more well-known mechanisms include hydrogen-enhanced localized plasticity (HELP) [8, 9, 10, 11], and hydrogen-enhanced decohesion (HEDE) [12, 13, 14]. The HELP mechanism posits that hydrogen helps facilitate the nucleation, motion, and build-up of dislocations, leading to localized plastic deformation and fracture. Meanwhile, HEDE suggests that the segregation of H to grain boundaries and cracks weakens the bonds between metal atoms thus making it easier to fracture. More recently, yet another mechanism was proposed by Song and Curtin, in which hydrogen accumulation at the crack tip simultaneously decreases the fracture energy and increases the barrier for dislocation emission, leading to a "ductile-to-brittle" transition at the crack tip [15, 16]. However, there is no clear consensus as to which mechanism is operative under a set of specific microstructural conditions, and it is widely believed that multiple mechanisms are at play simultaneously, and different mechanisms dominate in different materials and under different environmental conditions [17, 18, 19, 20, 21, 22].

Recently, a new class of metallic structural materials – complex concentrated alloys (CCAs), which include high entropy alloys and their derivatives, including medium entropy alloys and non-equiatomic multiprincipal element alloys – have attracted a lot of research interest due to their excellent mechanical properties such as high strength, ductility, and toughness [23, 24, 25, 26, 27]. Due to their generally low stacking fault energies [28, 29], CCAs from the Cantor alloy family [30]

tend to contain high density of nanotwins, and twinning-based deformation mechanisms have been credited for their excellent mechanical properties [31, 27]. Some studies have also reported potentially improved HE resistance in fcc CCAs such as CrCoNi [32, 33], CoCrFeMnNi [34, 35, 36], and CoNiV [37]. However, given the complexity of HE, and the differences in experimental conditions and sample microstructures employed in the different studies, a systematic understanding of HE in CCAs is still lacking. The presence of a high density of nanotwins has been suggested as one of the factors contributing to the improved HE resistance in some CCAs [34, 35, 37], although the exact mechanisms for this are not yet well understood. If shown to be true, this could present opportunities to further improve the HE resistance of CCAs via tailoring their microstructure to optimize their mechanical performance [38].

Due to the small size of hydrogen atoms, it is challenging to directly observe the diffusion and distribution of hydrogen in a sample experimentally. This is where simulations, and in particular, atomic level simulations, can help to provide insights into the details of various HE mechanisms. However, there have thus far been few efforts to study hydrogen behavior and HE in CCAs. A few first-principles density functional theory (DFT) studies have investigated the solution energies and diffusivity of hydrogen in CCAs, as well as the effect of hydrogen on stacking fault energies and surface energies, all of which are complicated by the wide variety of chemical environments that are possible in CCAs [39, 40, 41, 42, 43, 44]. Direct modeling of HE mechanisms is even more limited, due in part to the lack of reliable interatomic potentials to describe CCAs containing hydrogen which has thus far precluded molecular dynamics simulations of HE in CCAs. In a recent study, Zhou, Tehranchi and Curtin [45] presented a DFT-informed model based on Song and Curtin's mechanism which predicted the embrittlement of various stainless steels and face-centered cubic (fcc) CCAs in good agreement with existing experiments.

However, the abovementioned study only considered crack propagation in the fcc bulk matrix, and did not consider the effect of microstructural features such as twin boundaries (TBs) and other grain boundaries, which can have distinct embrittlement behavior compared to the bulk matrix. For example, Cheng *et al.* [46] investigated the intrinsic brittleness and ductility of grain boundaries in fcc Cu, and predicted a ductile-brittle anisotropy for crack propagation along certain coherent symmetrical tilt grain boundaries including the TB. Since twinning deformation mechanisms are believed to be responsible for the excellent mechanical properties in fcc CCAs [31, 27, 47], there

is interest in engineering highly nano-twinned or gradient nano-twinned structures for such materials [38, 48]. However, the effect of TBs on HE in such materials is not well understood and is somewhat speculative. Hence, we believe that it would be of value to study the interaction between cracks, hydrogen, and TBs in fcc CCAs, using CrCoNi as a model system, to try to gain some insight into the possible role of TBs on the HE of some alloys in the fcc CCA family.

In this work, following the general approach of Zhou, Tehranchi and Curtin [45], we have employed a DFT-informed Griffith-Rice model to predict the ductile or brittle response of a crack tip interacting with twin boundaries in CrCoNi CCA, both in the absence of and presence of atomic hydrogen at the crack tip. By comparing the conditions at the onset of the ductile-to-brittle transition, we predict the relative likelihood of embrittlement for different crack configurations: in the bulk matrix, along a TB, and impinging on a TB. We compare the crack-TB behavior in CrCoNi with a typical fcc metal, Ni, and also validate our model predictions with molecular dynamics (MD) simulations when possible. The details of the DFT calculations, Griffith-Rice crack prediction model, and MD simulations are described in Sec. 2. In Sec. 3.1, we first discuss the trends in the DFT-computed material properties as a function of the local hydrogen coverage. Next, we report the predictions from the DFT-informed Griffith-Rice model and MD simulations in the absence of hydrogen (Sec. 3.2.1), and in the presence of hydrogen (Sec. 3.2.2). Both the model and MD simulations predict that TBs in both fcc Ni and CrCoNi CCA could potentially improve HE resistance as it impedes advancement of an approaching crack while promoting dislocation emission along the TB. We discuss how the mechanism demonstrated in this study could help explain the improved HE tolerance of highly twinned CCAs such as CrCoNi in Sec. 4, and summarize the key observations in Sec. 5.

2. Methodology

2.1. DFT computational details

We perform first-principles density functional theory (DFT) calculations as implemented in the Vienna ab initio Simulation Package (VASP) [49, 50, 51]. We use projector-augmented wave potentials [52, 53] with valence electron configurations of $3d^7 4s^2$, $3p^6 3d^5 4s^1$, and $3p^6 3d^8 4s^2$ to model Cr, Co, and Ni respectively, and treat the exchange-correlation using the Perdew-Burke-Ernzerhof (PBE) [54] generalized gradient approximation (GGA) functional. We employed a

plane-wave cutoff energy of 420 eV, first-order Methfessel-Paxton smearing [55] of the Brillion zone with a smearing energy width of 0.10 eV, and Γ-centered Monkhorst-Pack k-point meshes [56] with k-point spacing of approximately 0.03 Å^{-1}. All calculations were performed with collinear spin polarization, allowing the magnetic moments on all atoms to be optimized along with the ionic coordinates.

We construct different types of atomistic models to evaluate the formation energy, stable and unstable stacking fault energies, twin boundary energy, and surface energy in CrCoNi CCA. We start by constructing multiple bulk supercells with different atomic configurations using the Alloy Theoretic Automated Toolkit (ATAT) [57]. The 48-atom special quasi-random structure (SQS) [58] supercells have supercell vectors $4\cdot\frac{a_0}{2}[1\bar{1}0]\times 2\cdot\frac{a_0}{2}[11\bar{2}]\times a_0[111]$). SQS with correlation functions as close to that in a random model are used to represent the random solid solution CrCoNi CCA, while a few other structures generated by the Monte Carlo algorithm [57] whose correlation functions deviate from the target random values, i.e., indicating some degree of non-randomness, are also selected to represent other possible CrCoNi structures with potentially some degree of short-range ordering.

The supercells for the stacking fault (SF), twin boundary (TB), and surface energy calculations are constructed by stacking the 48-atom supercells along the {111} direction and applying the relevant modifications as follows. The stable and unstable stacking faults are constructed in supercells of 4×48-atoms by shearing the supercell vector which is normal to the slip plane by $\frac{a_0}{6}[11\bar{2}]$ or $\frac{a_0}{12}[11\bar{2}]$, respectively, generating a single stacking fault per supercell separated from its periodic images by 12 {111} layers. The twin boundaries are also constructed in a 4×48-atom supercell, by mirroring the top 6 layers, creating two twin boundaries per supercell separated by 6 {111} layers. Finally, the {111} surfaces are modeled in a supercell containing a 3×48-atom slab and 15 Å of vacuum spacing. We evaluated the planar fault or surface energies at three different planes/surfaces in each supercell to sample the different local environments. Each structure is fully relaxed except for the unstable stacking faults, in which the ions are only allowed to relax in the direction normal to the slip plane. The energy of each fault or surface structure is referenced to the energy of the corresponding bulk structure from which it was constructed; for the unstable stacking faults, the reference structures were also only allowed to relax in the direction normal to the slip plane so that the excess energy due to the constrained relaxation may (somewhat) cancel out.

In addition, we also evaluate the above properties of CrCoNi in the presence of hydrogen. After verifying that the preferred interstitial sites for atomic hydrogen in the fcc lattice are the octahedral intersititat sites, we insert one or more hydrogen atoms into octahedral interstitial sites in the bulk, stable stacking fault, twin boundary, or on the surface. In the unstable stacking fault, the stable interstitial sites are found to be a sort of distorted tetrahedral site which is an intermediate between the stable octahedral sites in the bulk and stable stacking fault structures. The hydrogen solution energy in bulk is evaluated as

$$E_{\text{bulk}}^{\text{sol}} = E_{\text{bulk+H}} - E_{\text{bulk}} - \frac{1}{2}E_{\text{H}_2} \tag{1}$$

where $E_{\text{bulk+H}}$ and E_{bulk} are the energies of a bulk supercell with and without a H atom in an octahedral site, and E_{H_2} is the energy of a Hydrogen molecule. The hydrogen solution energy in the stacking fault and twin boundary are evaluated similarly. The planar fault and surface energies are also evaluated at 50% and 100% H coverage on the respective fault plane or surface, referenced to the corresponding unfaulted structures with the same level of H coverage.

2.2. Crack prediction model

We follow the general approach laid out by Zhou, Tehranchi and Curtin [45], in which they modeled the crack tip response by considering the competition between brittle cleavage and dislocation emission from an atomically sharp crack tip via a Griffith-Rice model. This approach has been used to predict the intrinsic ductility of materials [59, 60, 1] as well as at grain boundaries [61, 62, 46]. We employ the same approach to predict the response of a crack tip in bulk CrCoNi (for comparison with Zhou, Tehranchi and Curtin's work), followed by extending the analysis to crack tips along and approaching a twin boundary. To simplify the problem for analysis, we will assume the existing crack to be under Mode I loading.

In Griffith's theory of brittle fracture [63], the energy release rate for brittle cleavage G_{cleave} along a twin boundary is given by

$$G_{\text{cleave}} = 2\gamma_{\text{surf}}^{F} - \gamma_{\text{TB}} \tag{2}$$

where γ_{surf} is the free energy of the surface and γ_{TB} is the twin boundary energy.

Meanwhile, in Rice's model [1], the energy release rate for dislocation emission from a crack

tip under Mode I loading, G_{emit}, is given by

$$G_{\text{emit}} = 8\gamma_{\text{USF}} \frac{1 + (1-\nu)\tan^2\phi}{(1+\cos\theta)\sin^2\theta} \tag{3}$$

where γ_{USF} is the unstable stacking fault energy, ν is Poisson's ratio, ϕ is the orientation of the Burgers vector, and θ is the angle of inclination between the crack plane and dislocation slip plane, as illustrated schematically in Figure 1(a). For a given crack orientation, if G_{cleave} is less than G_{emit}, the crack will propagate in a brittle manner, whereas if G_{emit} is less than G_{cleave}, the crack will tend to emit dislocations and blunt instead.

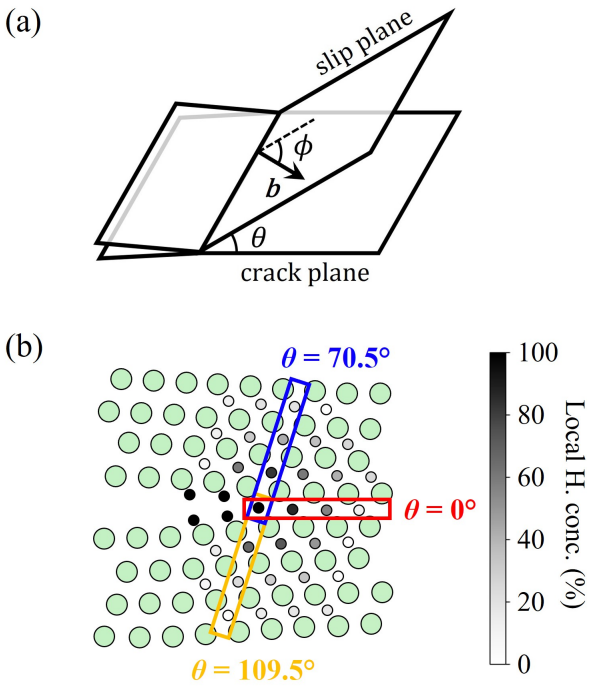

Figure 1: (a) Schematic illustrating the geometry of dislocation emission from an atomically sharp crack. The slip plane and dislocation Burgers vector orientation are defined by angles θ and ϕ, respectively. (b) Schematic illustrating the H segregation at a crack tip, and the sites used to estimate the local H concentrations on the slip and cleavage planes of interest. Matrix atoms are depicted as larger green circles, while the octahedral interstitial sites near the crack tip are depicted as small circles, shaded according to the local H concentration.

Zhou, Tehranchi and Curtin considered the role of H in driving an intrinsic ductile-to-brittle transition at a crack tip by preventing dislocation emission and crack tip blunting, while promoting cleavage. Following their approach, we model the segregation of H at a crack tip by assuming that under applied stress intensity K_I^{app}, H migrates towards the crack tip due to the (hydrostatic)

pressure field around the crack tip. For a crack under Mode I loading, this is approximated as

$$p_i(r_i, \theta_i) = \frac{2(1+\nu)K_I^{\text{app}}}{3\sqrt{2\pi r_i}} \cos\frac{\theta_i}{2} \tag{4}$$

at position (r_i,θ_i) relative to the crack tip [64]. The H concentration at position (r_i,θ_i) is then evaluated as the integral of the density of states of H absorption sites, $n(E^{\text{sol}})$, and the Fermi-Dirac occupation function:

$$c_i = \int_{-\infty}^{+\infty} \frac{n(E^{\text{sol}})\, dE^{\text{sol}}}{1 + \exp(\frac{E^{\text{sol}} - p_i V_m + E_{\text{ZP}} - \mu}{k_B T})} \tag{5}$$

where V_m is the average misfit volume of a H atom in an octahedral interstitial site, E_{ZP} is the H zero-point energy, μ is the H chemical potential, and $k_B T$ is the available thermal energy at temperature T. Unless otherwise specified, we use $V_m = 2.8$ Å^3 and $E_{\text{ZP}} = 0.18$ eV, following Zhou *et al.* [45], which allows us to compare our predictions for the bulk case. We evaluate the model at $T = 300$ K, corresponding to the room temperature at which tensile testing has been carried out in experiments [33, 65, 32]. The grey shading of the octahedral interstitial sites in Figure 1(b) shows an example of the H concentration distribution around a crack tip under the specific conditions of 1380 appm average bulk H concentration and applied stress intensity factor $K_I^{\text{app}} = 0.8$ MPa m$^{1/2}$.

While the segregation of H atoms at the crack tip is energetically favorable, it comes at a cost to the entropy of the overall system. The main contribution to this is the change in the configurational entropy γ^S_{surf} due to moving H atoms from the bulk to the crack tip surface sites, which is given by

$$\gamma^S_{\text{surf}} = \frac{k_B T}{A_0}[(1 - C_s)\ln(1 - C_s) + C_s \ln C_s - C_s \ln C_b] \tag{6}$$

where A_0 is the area per surface site, C_s is the H coverage on the surface, and C_b is the bulk H concentration. The entropy is accounted for in the free energy of the surface $\gamma^F_{\text{surf}} = \gamma^E_{\text{surf}} + \gamma^S_{\text{surf}}$ in Eqn. (2), where γ^E_{surf} is the surface energy computed from DFT. For the bulk H concentrations and temperatures evaluated in this work, the entropy contribution is around 0.2 eV at 50% coverage and 0.4–0.5 eV at 100% coverage.

Due to the chemical inhomogeneity of CCAs, all the material properties – including the local surface energy γ_{surf}, twin boundary energy γ_{TB}, unstable stacking fault energy γ_{USF} and H solution energies – vary spatially. The length scale over which the fluctuations in local material properties

affects the material behavior has been found to depend on the critical length scale of the underlying mechanism(s) [66]. In our model, the relevant mechanisms are the dislocation nucleation and brittle crack opening processes. Previous modeling work found that the critical loop size for dislocation nucleation in CrCoNi tends to fall between 4–6 Å [66]. For the ideal brittle cleavage process as described by Griffith, the associated length scale is the size of the fracture process zone, which is typically on the order of a few atomic lattice spacings (≈ nm). Our DFT calculations yield planar fault and surface energies averaged over the cross-sectional area of the DFT supercell, approximately 10.0 Å × 8.6 Å ≈ 86 $Å^2$, corresponding to the area of a circular loop of radius approximately 5.2 $Å^2$. Hence, we believe that the various length scales in our model and DFT calculations are consistent, and the distributions of the DFT-computed local properties do not need to be re-scaled.

The various material properties which are inputs to Eqns. (2) and (3) also vary as a function of the local H concentration. As shown by the grey shading in Fig. 1(b), H tends to accumulate near the crack tip which experiences the largest tensile strain under mode I loading. Furthermore, we note that the elevated local H concentration extends from the crack tip for 5-10 Å, or equivalent to a few lattice spacings. We estimate the local H concentration by averaging the H concentration along the slip or cleavage planes of interest, as illustrated by the colored boxes in Figure 1(b). We average the H concentrations over a distance of around 1 nm from the crack tip (equivalent to 4 atomic lattice spacings) to be consistent with the length scales described above. This gives us a definition for the average local H coverage on the surface/fault plane which is consistent with that in our DFT calculations. The averaged H concentrations in the relevant regions are then used to estimate the change in γ_{surf}, γ_{TB}, and γ_{USF} in the presence of H. The sites we have chosen for averaging the local H concentrations are slightly different from that in Zhou *et al.* [45], which leads to some differences in the quantitative predictions. In our study, we found that assuming the H coverage on the fracture surface to be half of that on the pre-cleavage plane was sufficient to predict embrittlement, i.e., we did not have to assume nanodiffusion of H to crack tip sites as they did. We compare our results with Zhou *et al.* in greater detail in the results sections.

2.3. Molecular dynamics simulations

We performed molecular dynamics (MD) simulations using the large-scale atomic/molecular massively parallel simulator (LAMMPS) [67] to study the crack propagation under Mode I load-

ing in typical random CrCoNi system and Ni-H system to unveil the influence of twin boundary and H solute on the crack propagation behavior. Widely used Embedded-atom method (EAM) interatomic potentials for CrCoNi [68] and Ni-H systems [69] were adopted in this study. Due to the lack of a reliable interatomic potential for the CrCoNi-H system, we used the Ni-H system as a model system to study HE at TB in fcc alloys. To model the crack propagation behavior, we created cylinder samples with axis along the [111] direction and in-plane radius of 20 nm. A single twin boundary is introduced in each sample if required, and atomically sharp cracks are created in the simulation samples by removing the interaction between atoms across the crack plane. A schematic of the simulation setup is depicted in Fig. S3. Atoms at the boundary of the cylinder samples were deformed according to the displacement field obtained from the K field at crack tip from linear elasticity theory [70]. CrCoNi samples were created by randomly replacing two-thirds of the Ni atoms in a face-centered cubic (fcc) Ni sample with an equal number of Co and Cr atoms. Periodic boundary condition was adopted only in the axis direction and temperature was set at 5 K in all crack propagation simulations to reduce thermal fluctuations and allow the investigation of the intrinsic ductile/brittle behavior at crack tips. For the hydrogen embrittlement simulations in the Ni-H system, due to time scale limitations, the kinetics of H atoms (i.e., diffusion and equilibration of H atoms around the crack tip) are not explicitly included. Instead, as an approximation, H atoms are inserted into all the octahedral sites within around 8 Å of the crack tip region before the Mode I loading. The loading rate of all the simulation is 1 MPa $\sqrt{\text{m}}$/ns.

3. Results

3.1. DFT-computed properties

Planar fault energies vs. H content:

We consider the effect of 50% and 100% H coverage on the planar fault and surface energies. Evaluating 100% H coverage is straightforward – we simply occupy all possible stable interstitial sites at the fault plane/surface with H atoms and compute the fault energies as before. The 50% H coverage is evaluated based on randomly occupying half the possible stable interstitial sites at the fault plane/surface. However, this overestimates the energies slightly as it does not reflect the thermodynamic occupation of sites. Zhou *et al.* [45] estimated that this overestimation was on the order of 5% for the surface energy of CoCrFeMnNi. Assuming a similar degree of overestimation

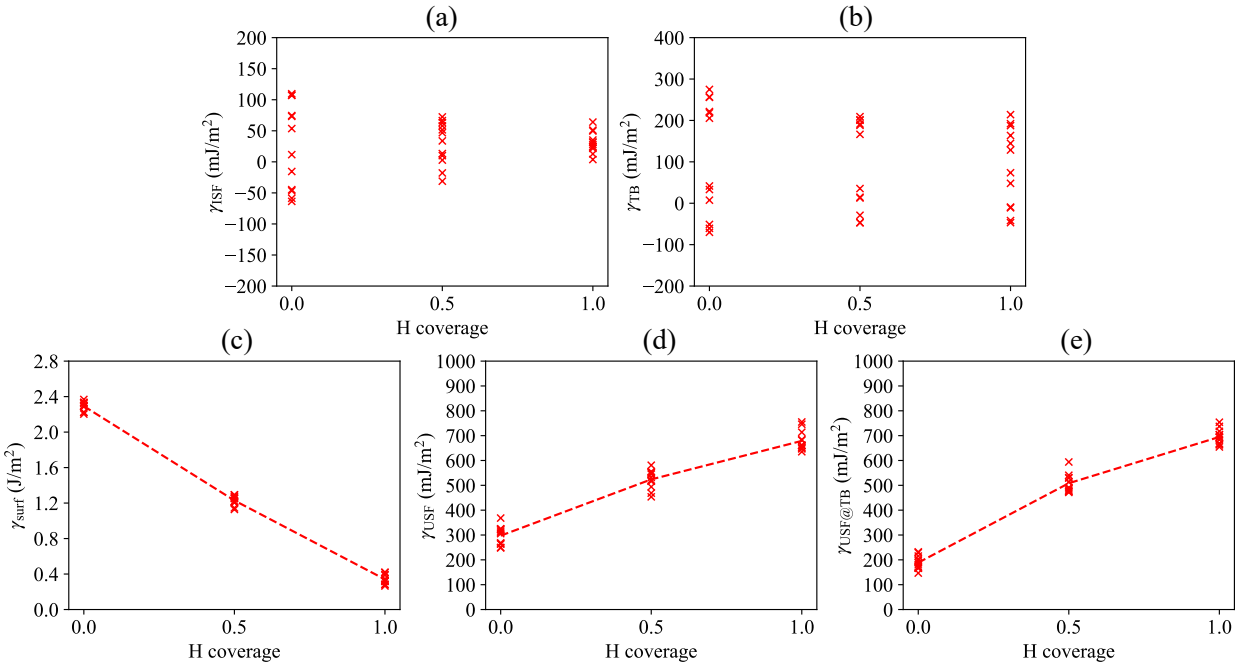

Figure 2: Summary of DFT-computed properties: (a) intrinsic stacking fault energy γ_{ISF}, (b) twin boundary energy γ_{TB}, (c) {111} surface energy γ_{surf}, (d) unstable stacking fault energy γ_{USF}, (e) energy of unstable stacking fault at twin boundary $\gamma_{USF@TB}$. For a given H coverage, γ_{ISF} and γ_{TB} show a relatively large scatter in their values depending on the initial structure, while γ_{surf}, γ_{USF}, and $\gamma_{USF@TB}$ show relatively less scatter. While γ_{ISF} and γ_{TB} do not, on average, show a clear trend vs. H coverage, γ_{surf} always decreases while γ_{USF} and $\gamma_{USF@TB}$ always increases with increasing H coverage.

in our planar fault energies does not change the general trends observed, hence we report the energies for random 50% coverage in Figs. 2.

Both the intrinsic stacking fault energy (γ_{ISF}) and twin boundary energy (γ_{TB}) show a significant scatter in their values depending on the local chemical environments in their initial structures. The scatter in γ_{ISF} decreases with increasing H coverage as the layer of H atoms inserted at the fault plane somewhat disrupts the chemical bonding across the fault plane, hence reducing the effect of the different local chemistries. That said, on average, γ_{ISF} and γ_{TB} do not show distinct trends vs. H coverage.

In contrast, the unstable stacking fault energies (γ_{USF}) and {111} surface energy (γ_{surf}) show relatively less scatter with respect to their local chemical environments, and whether or not these local environments may contain some degree of short-range ordering. It is likely that the energetic contributions to these energies is dominated by the highly unfavorable structural environments rather than chemical effects which are relatively smaller. Unsurprisingly, γ_{USF} increases and γ_{surf} decreases with increasing H coverage, and our results are generally consistent with those reported by Zhou *et al.* [45]. At high H coverage, our average γ_{surf} is somewhat less than that reported by Zhou *et al.* (0.36 vs. 0.59 J/m^2), which may arise due to differences in the choice of structures, slight differences in the magnetic states, etc. The impact on our model's predictions is limited since our model is concerned with H surface coverage up to 50%, for which the differences between our DFT-computed data are smaller.

Finally, it is worth noting that we differentiate between an unstable stacking fault originating in a bulk matrix ("USF") and an unstable stacking fault on a twin boundary ("USF@TB"); we find the latter to have a slightly lower energy barrier for dislocation emission along an existing twin boundary, which has implications on the behavior of a crack approaching a twin boundary.

Hydrogen solution energy distributions:

Figure 3 depicts the distributions of H solution energy at octahedral sites in the bulk and at a twin boundary. Each distribution was evaluated based on inserting individual H atoms at 40 – 50 interstitial sites at random in different supercells. We did not observe any clear differences in the H solution energy evaluated in different supercells, hence the data are combined and treated as a single distribution each in bulk and at the twin boundary. The dashed vertical lines indicate the mean of each distribution, the dashed curves are the kernel density estimation of the raw his-

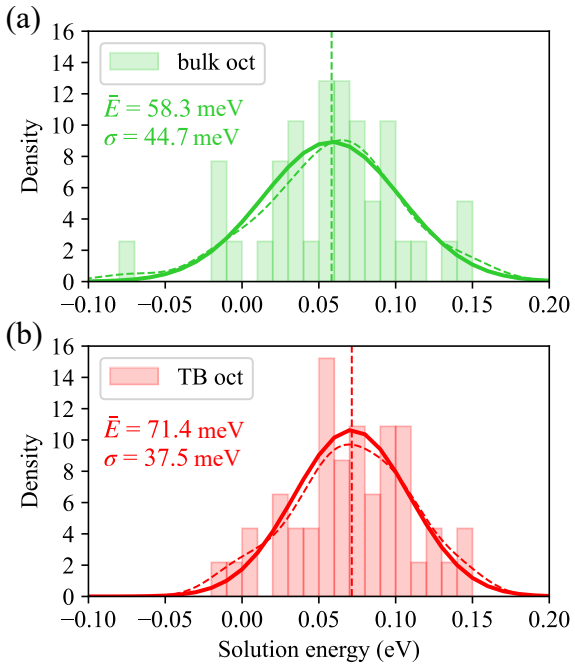

Figure 3: Distributions of the H solution energy in CrCoNi (a) bulk and (b) twin boundary. The histograms show the H solution energies evaluated in 40-50 randomly-chosen octahedral sites, with the dashed curve representing the kernel density estimate (smoothed histogram) of the raw data and the vertical dashed line indicating the distribution mean. For comparison, the solid curve shows the best fit Gaussian distribution in each case, with mean $\bar{E}$ and standard deviation σ as indicated. The distributions of H solution energies do not suggest an energetic driving force for H segregation to twin boundaries in CrCoNi.

tograms, and the solid curves represent a Gaussian distribution with mean $\bar{E}$ and standard deviation σ fit to the data. The solution energy distributions (i.e., density of states $n(E^{\text{sol}})$) in bulk and at the twin boundary appear to closely follow Gaussian distributions, hence we will represent them by Gaussian distributions with the appropriate mean and standard deviation when evaluating Eqn. (5). We find that the average solution energies for a H atom in the twin boundary are in fact slightly higher than that in bulk, which suggests that H would not tend to segregate to twin boundaries in CrCoNi.

3.2. Crack modeling

Figure 4 illustrates schematically the different crack orientations considered in this work: a crack in the bulk matrix, a crack along a twin boundary, and a crack impinging on a twin boundary. We consider cracks propagating along {111} planes as these are the most energetically favorable surfaces. The twin boundary also lies along a {111} plane, hence such cracks could propagate along the twin boundary. Due to the mirroring of the lattice above and below the twin boundary, there are two inequivalent directions ($\delta = 0°$ and $180°$) for a crack along the twin boundary (b, d). Based on the relative orientations of {111} planes in an fcc lattice, a {111} crack impinging on a twin boundary does so at an angle of $\delta = 70.5°$, as depicted in subfigure (c).

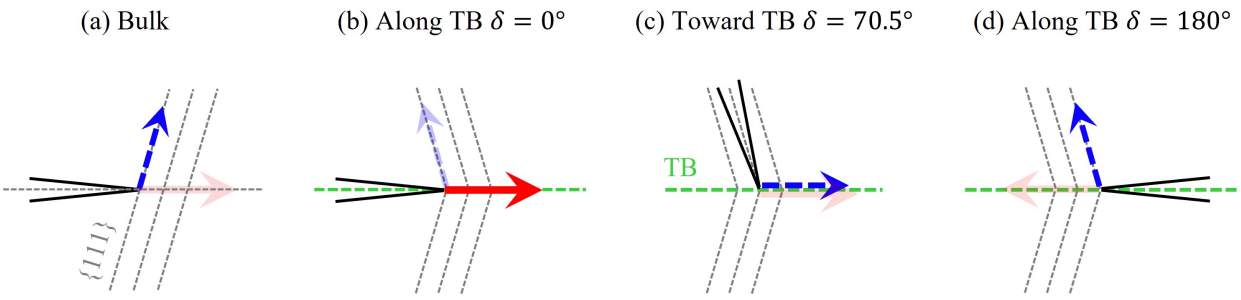

Figure 4: Schematic figures illustrating the competing mechanisms considered for crack propagation (a) in CrCoNi bulk matrix, (b, d) along a twin boundary, and (c) towards a twin boundary. The blue dashed arrows indicate possible dislocation emission directions, the red solid arrows possible crack cleavage directions, the green dashed lines the twin boundary, and the thin black dashed lines {111} planes. The arrows indicating the predicted dominant mechanism (dislocation emission or cleavage) are drawn in bold.

3.2.1. Without Hydrogen

Table 1 summarizes the predicted G_{emit} and G_{cleave} evaluated for different crack configurations. Since we found that the dominant terms controlling the cleavage and dislocation emission processes (γ_{surf}, γ_{USF}, $\gamma_{\text{USF@TB}}$) don't have strong dependence on short-range ordering, attempts to

	Bulk	Along TB $\delta = 0°$	Toward TB $\delta = 70.5°$	Along TB $\delta = 180°$
θ (°)	70.53	109.47	70.53	70.53
ϕ (°)	0	60	0	0
G_{emit} (J/m^2)	2.00 (1.67-2.48)	12.32 (10.27-15.26)	1.27 (1.00-1.57)	2.00 (1.67-2.48)
G_{cleave} (J/m^2)	4.58 (4.41-4.74)	4.47 (4.13-4.81)	4.47 (4.13-4.81)	4.47 (4.13-4.81)
Prediction	Disl. emission	Cleavage	Disl. emission	Disl. emission

Table 1: Calculated G_{emit} for dislocation nucleation based on Rice's model, and G_{cleave} for cleavage based on Griffith's model, for a crack in the bulk matrix, along a twin boundary (TB), and towards a TB in CrCoNi. The relevant competing mechanisms considered in each case are illustrated in Figure 4. In the "Toward TB" case, the G_{emit} and G_{cleave} listed are for dislocation emission and cleavage along the TB at $\delta = 70.5°$. G_{emit} and G_{cleave} for other possible mechanisms are listed in the SI. The values not in parentheses have been evaluated using the averages of our DFT-computed input data, while the values in parentheses indicate the possible range of values based on the minimum and maximum values from our input data sets.

account for short-range ordering lead to similar predictions from the Griffith-Rice model. Furthermore, since the presence and degree of short-range ordering in CCAs is still unconfirmed experimentally, it could even be argued that short-range ordering should not be a consideration in the model in the first place. Due to these reasons, throughout the rest of this work we will not consider the effects of short-range order on the embrittlement of CrCoNi.

In the bulk matrix, we predict that a crack can propagate in a ductile manner as there is always a favorable set of {111} planes for dislocation emission on one side of the crack plane. However, similar to what had been predicted and observed in simulations in fcc Cu [46], the model here also predicts a directional anisotropy for crack propagation along the twin boundary. In one direction ($\delta = 0°$), brittle cleavage is favored as the orientation of the {111} planes in both grains is not favorable for dislocation emission. Meanwhile, a crack travelling along the twin boundary in the opposite direction ($\delta = 180°$) may propagate in a ductile manner similar to that in the matrix, as the {111} planes are oriented favorably relative to this crack propagation direction. Finally, for a crack approaching the twin boundary at $\delta = 70.5°$, the model predicts that the emission of dislocations along the twin boundary is preferred over both intergranular decohesion and transgranular cleavage.

Figure 5 shows the MD verification of the model predictions on the interaction between a crack tip and TB in CrCoNi under different configurations. For a crack along the TB, in the $\delta = 180°$ case, the MD simulation agrees with the model which predicts dislocation emission as the dominant mechanism (i.e., ductile behavior). However, in the $\delta = 0°$ case, in contrast to the model prediction of brittle cleavage, MD simulations predict dislocation emission on other inclined

{111} slip planes as shown in the supplementary figure S4. This may be due to the presence of additional internal lattice strains due to the chemical inhomogeneity which activate additional slip systems not considered by the simple Rice model. For the case of a crack approaching a TB, a twinning partial dislocation will emit from the crack tip along the TB and induce TB migration as predicted by the model. We observe that in some simulations, after nucleating, dislocations do not immediately propagate away, but appear temporarily "pinned" near the crack tip. This is due to the variation in local stacking fault energy in CCAs: dislocations nucleate first in a region of low local stacking fault energy, but face a higher barrier to propagate through a region of high local stacking fault energy.

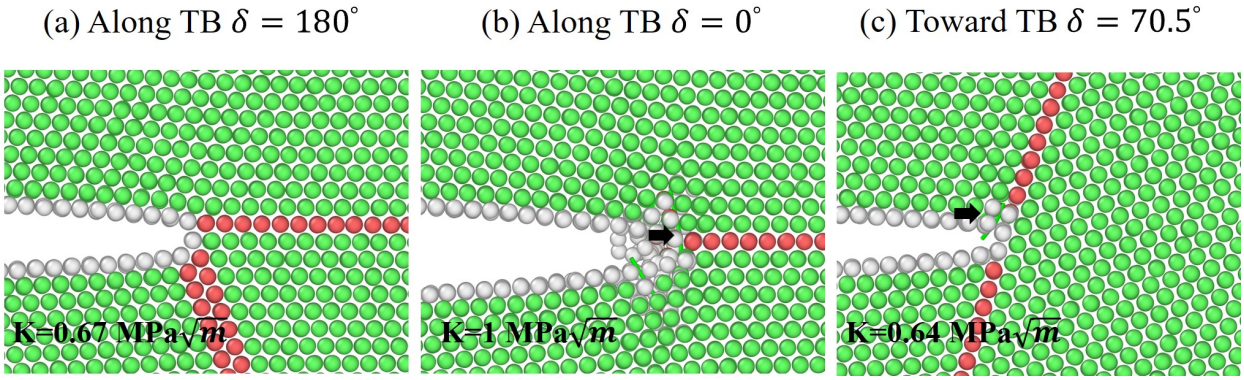

Figure 5: Crack tip atomic structure in CrCoNi at different K_I^{app} (a) along the "ductile" direction of a TB, (b) along the "brittle" direction of a TB and (c) towards a TB. Atoms with fcc, hcp, and unknown coordination are colored green, red, and white, respectively. The twin boundary and stacking fault trailing an emitted partial dislocation have locally hcp-like structure, hence appear as red atoms. Green line represents Shockley partial dislocation, whose location is indicated by the black arrows in (b) and (c).

3.2.2. With Hydrogen

We consider the three crack configurations which are predicted by the model to be ductile in the absence of hydrogen, and for which the model predictions have been verified by MD simulations: a crack in the bulk matrix, along a TB ($\delta = 180°$), and approaching a TB ($\delta = 70.5°$).

In all cases, the presence of H leads to embrittlement as H reduces γ_{surf} and increases γ_{USF} and $\gamma_{\text{USF@TB}}$. We use the model to estimate the conditions for embrittlement in each case. For comparison purposes, G_{cleave} and G_{emit} evaluted using Eqns. (2) and (3) have been converted to K_{Ic} and K_{Ie} respectively using the relation $K_I = \sqrt{EG/(1-\nu^2)}$. Figure 6 (a)-(c) plot the variation in K_{Ic} and K_{Ie} as a function of K_I^{app}, for the three different orientations of a crack in bulk (a), along a twin boundary (b), and towards a twin boundary (c), for average bulk H concentration

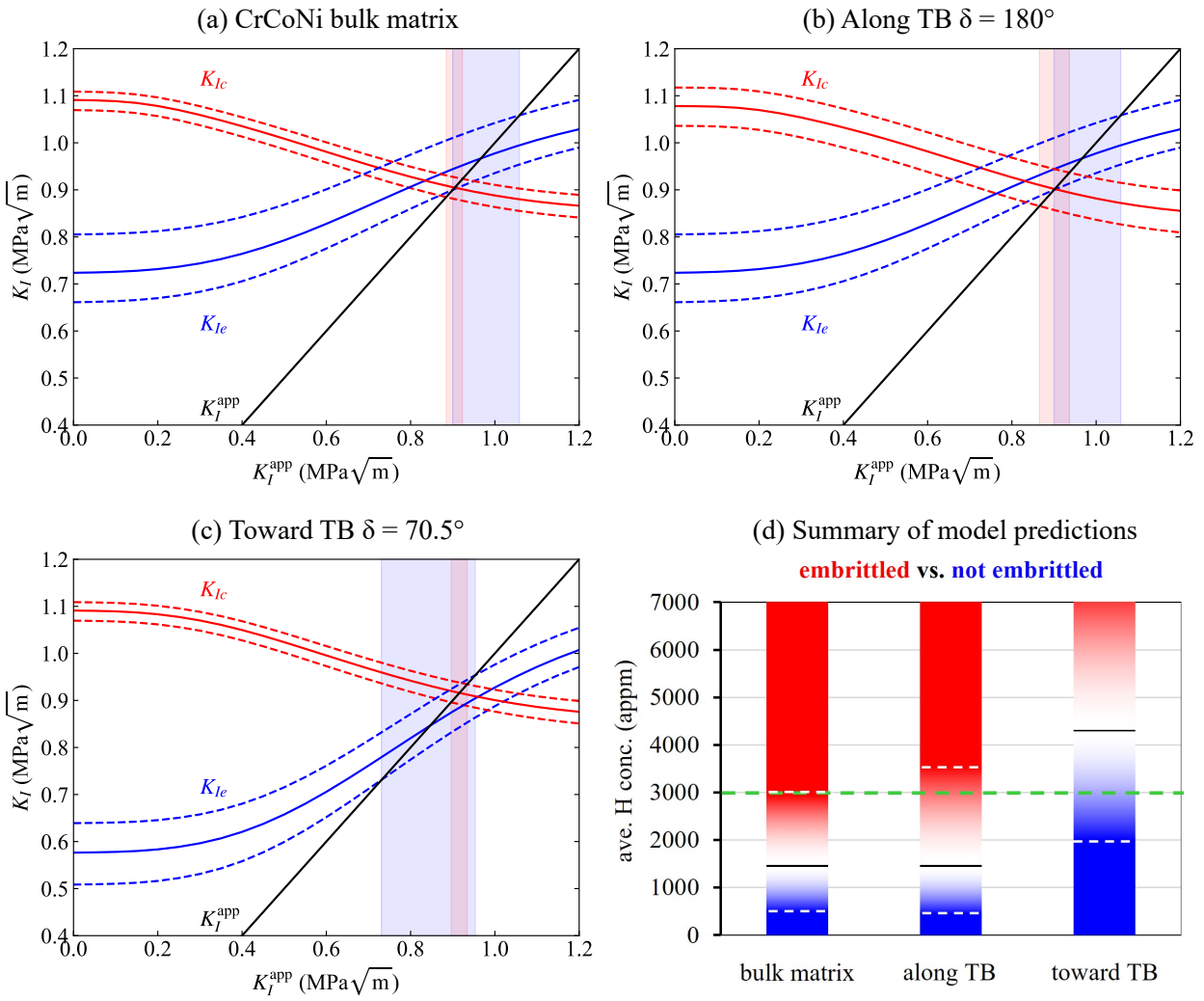

Figure 6: Model predictions of embrittlement in (a) CrCoNi bulk matrix, (b) along a twin boundary, and (c) towards a twin boundary, at a bulk H concentration of 3000 appm and $T = 300$K. The red and blue shaded regions indicate the ranges of K_I^{app} which may intersect the K_{Ic} and K_{Ie} curves respectively, which activates the corresponding mechanism at the crack tip. Under these conditions, the model predicts that a crack in the bulk matrix or along a TB will likely cleave in a brittle manner, while a crack approaching a TB is more likely to emit dislocations along the TB. (d) Summary of model predictions. The red (blue) sections of the bars indicate the range of average bulk H concentrations which would (would not) lead to embrittlement at a crack tip in each of the three cases. The green dashed line indicates the conditions corresponding to the plots shown in (a)–(c).

$C_b \approx 3000$ appm and $T = 300$ K. The solid curves indicate the K_{Ic} and K_{Ie} values evaluated using the averages of our DFT-computed input data, while dashed curves indicate the range of K_{Ic} and K_{Ie} values based on the minimum and maximum values from our input data sets. The red and blue shaded regions indicate the ranges of K_I^{app} which intersect the K_{Ic} and K_{Ie} curves, respectively. If K_I^{app} intersects K_{Ic} before K_{Ie} (as in subfigure (a)), then we predict that the crack will tend to cleave, whereas if K_I^{app} intersects K_{Ie} before K_{Ic}, we would predict that the crack will tend to emit dislocations. Under some conditions, variability in the input material properties (e.g., γ_{surf}, γ_{USF}, E^{sol}) lead to uncertainty whether K_I^{app} will intersect K_{Ie} or K_{Ic} first (blue and red shaded regions overlap, as in subfigure (c)). The uncertainties in the K_{Ie} and K_{Ic} reflect the local fluctuations which may temporarily retard or deflect the crack, similar to an impurity or inclusion in the matrix.

Figure 6 (d) summarizes the predictions from the model in each of the three cases considered. On each bar, the red and blue shading indicate the ranges of bulk H concentration for which the system is predicted to be embrittled versus not embrittled. The black horizontal line indicates the critical H concentration for the ductile-brittle transition as estimated based on the averages of our DFT-computed input data, while the white dashed lines indicate the region within which the prediction may be uncertain. Due to the variability in the input material properties, this region of uncertainty can be quite large. The green dashed line indicates the bulk H concentration (3000 appm) corresponding to the plots in (a)-(c): under these conditions, the model predicts that a crack in bulk or along a twin boundary is most likely to cleave in a brittle manner, while a crack approaching a twin boundary is somewhat more likely to emit dislocations.

Overall, the model predicts that a crack in the bulk matrix undergoes a "ductile-to-brittle" transition at bulk H concentrations C_b greater than $\approx$ 1500 appm (equivalent to $\approx$ 26.5 wppm in CrCoNi) on average, which is on the low end of the $\approx$ 1500 – 3000 appm range predicted by Zhou *et al.*;. The differences between our models' predictions arise primarily due to the different methods of estimating the local H coverage, as illustrated in Fig. 1(b). For a given K_I^{app}, due to the different definition of local H coverage, our model evaluates a higher (less reduced) surface energy and a higher (more increased) unstable stacking fault energy compared to Zhou *et al.*'s model. These two effects partly compensate, so that our final model prediction largely overlaps with Zhou *et al.*'s for the bulk case, but with the lower bound of the range of uncertain prediction extending to $C_b < 1000$ appm.

Along the TB, in the previously "ductile" direction ($\delta = 180°$), embrittlement is predicted under similar conditions as in bulk. This is because $\gamma_{TB} << \gamma_{surf}$ and E_{TB}^{sol} is similar to E_{bulk}^{sol}, meaning that the TB appears almost "invisible" to the crack propagating along it in this direction. In contrast, we predict that a crack approaching the TB is more likely to emit dislocations parallel to the TB, hence retaining its ductile property up to a higher $C_b \approx 4300$ appm (equivalent to ≈ 76 wppm in CrCoNi) on average. Crack tip blunting caused by dislocation emission, which is not considered in the model, could further alleviate the driving force for cleavage. When cleavage ultimately occurs, it may occur transgranularly due to the higher H accumulation in front of the crack tip than along the twin boundary.

We perform MD simulations to further verify the role of TB in the hydrogen-crack tip interaction as predicted by our model. Due to the lack of a reliable interatomic potential for CrCoNi-H system, we use fcc Ni as a model system to study hydrogen embrittlement at TB. Figure 7 shows the results of the MD simulations without hydrogen (first two rows) and with hydrogen (last row), allowing us to compare the crack responses in each of the three crack configurations for which the model has been evaluated.

In the absence of hydrogen, MD simulations predict dislocation emission from the crack tip at K_I^{app} of 0.53 MPa $\sqrt{m}$, 0.52 MPa $\sqrt{m}$, and 0.49 MPa $\sqrt{m}$ for a crack in the bulk, along the TB and towards the TB, respectively (Figure 7(ii)). Thus, the behavior of a crack in fcc Ni along these directions is similar to that observed in MD simulations of fcc CrCoNi (c.f. Fig. 5), and also in agreement with the model predictions for both CrCoNi and Ni (c.f. Fig S5). This suggests that the fundamental mechanisms in CrCoNi and Ni are similar, hence we believe that simulations of the Ni-H system should be able to provide insights into CrCoNi-H system as well.

When H atoms are present at the crack tip in Ni, crack advance is observed before dislocation emission for the crack in bulk (Figure 7(a)(iii)) and along a TB (Figure 7(b)(iii)). The crack advancement occurs at higher K_I^{app} than dislocation emission in the cases without hydrogen. For the case of a crack approaching a TB, dislocation emission and TB migration is observed before crack advancement. The crack tip is blocked by the TB due to the change of crystal orientation across the TB. These observations from MD simulations support our model predictions that under the same conditions, a crack impinging on a TB is less easily embrittled than a crack in the bulk matrix or along a TB, in both CrCoNi and Ni (c.f. Fig S5).

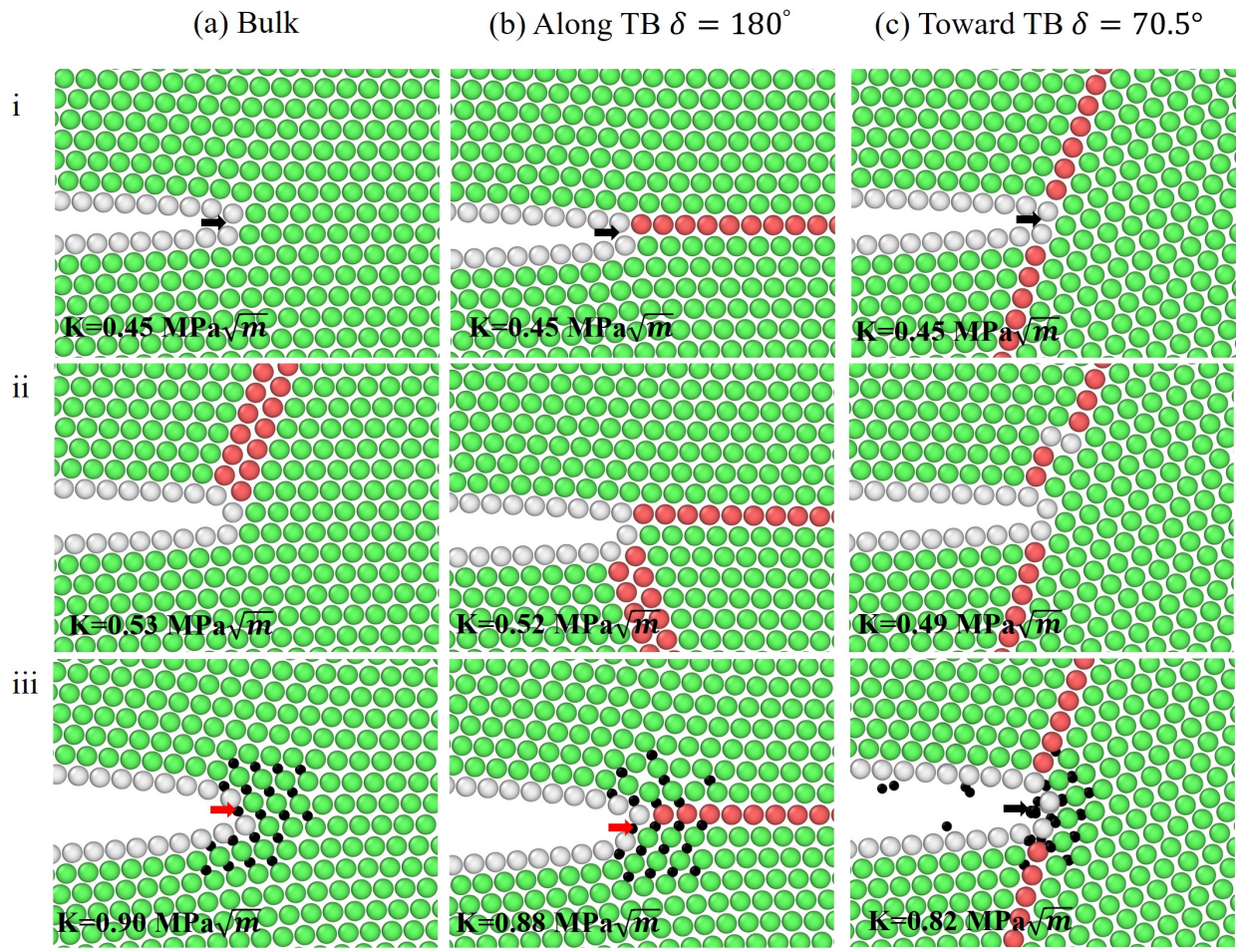

Figure 7: Crack tip atomic structure in fcc Ni at different K_I^{app} (a) in bulk matrix, (b) along the ductile direction of a TB and (c) towards a TB. Figures in row (i) and (ii) show the crack tip structure for pure Ni prior to and upon dislocation emission, respectively, while row (iii) shows the crack responses when hydrogen atoms were inserted at octahedral sites around the crack tips. Atoms with fcc, hcp, and unknown coordination are colored green, red, and white, respectively. Hydrogen atoms are colored black. Black arrows indicate the original location of the crack tip while red arrows indicate the new crack tip location after crack advance.

4. Discussion

Summarising our results, the Griffith-Rice model we have employed in this work predicts that TBs could help improve the HE resistance of fcc metals, in particular, by arresting approaching cracks and promoting dislocation emission along the TB, even in the presence of hydrogen at the crack tip. Where possible, we have verified our model predictions against molecular dynamics simulations, and find good agreement in nearly all cases. For the three crack configurations which are predicted to be ductile in the absence of hydrogen, i.e., a crack in bulk, along a TB ($\delta = 180°$), and towards a TB ($\delta = 70.5°$), the model and MD simulations agree well, with both predicting the same trend in embrittlement tendency. The only case for which the model predictions and MD simulations did not agree was for the case of a crack along the TB ($\delta = 0°$) in CrCoNi, which we address below.

Under the assumptions of the Rice model, twin boundaries are predicted to be more intrinsically brittle than the matrix due to the unavailability of favorable slip planes for dislocation emission in one of the directions. This ductile-brittle anisotropy has been observed in MD simulations of fcc metals like Cu [46] and Ni (this work). However, in CrCoNi, along the "brittle" direction, dislocations are observed to be emitted on a different (oblique) slip plane. This may be due to the presence of additional internal lattice strains due to the chemical inhomogeneity which activate alternative slip planes other than those considered by the Rice model. The activation of different slip systems at crack tip has also been reported in pure copper due to elevated temperature [71]. This illustrates a limitation of the standard Rice model which assumes the preferred slip system for dislocation emission based solely on the underlying fcc lattice.

Along the "ductile" direction, twin boundaries do not appear to be more susceptible to embrittlement than the bulk matrix in either CrCoNi or Ni. Furthermore, we predict that a (mode I) crack approaching a twin boundary may be temporarily arrested by the twin boundary, preferring to emit dislocations along or parallel to the twin boundary instead of continuing to propagate in a brittle manner. Due to the change in crystal orientation across the TB, the crack would need to deflect, which also helps slow it down. The emission of dislocations parallel to the twin boundary is observed in MD simulations in both Ni and CrCoNi without H; and in Ni with H. Hence, our simple model and MD simulations suggest that twin boundaries in fcc metals including CrCoNi are not more susceptible to embrittlement, and may even help improve HE resistance. The key

factors contributing to this are: (1) low twin boundary energy, (2) slightly lower intrinsic energy barrier for slip along an existing twin boundary than in the bulk matrix which reduces K_{Ie} at low to moderate H concentrations, and (3) similar H solubility at twin boundary vs. in the bulk matrix not leading to much H segregation along twin boundary.

These insights suggest that twin boundary engineering could be used to improve the performance of these metals without compromising on the HE resistance, unlike other grain boundary (GB) refinement approaches. Compared to TBs, other GBs tend to promote more H segregation [72], and to be more susceptible to GB embrittlement as a result [73]. This has actually been demonstrated in Ni – microstructures comprising a higher fraction of special boundaries (principally twin boundaries) compared to other types of GBs displayed less embrittlement compared to microstructures containing much lower special fractions, consistent with a lower proportion of intergranular fracture [74]. Seita *et al*. [75] found that while TBs in a Ni-base superalloy were more susceptible to crack initiation, they were more resistant to crack propagation compared to other GBs. To our knowledge, while similar approaches to improving HE resistance through microstructural design have yet to be demonstrated in fcc CCAs, we believe that given their low stacking fault energies and high twinnabilities, such systems could be well suited to applying grain boundary engineering and manipulating twin boundaries to improve their HE resistance.

Next, we attempt to compare our model predictions to experimental observations of HE in CrCoNi and related CCAs. In recent years, there have been a few experimental studies of HE in CrCoNi: Yi *et al.* [33] and Chen *et al.* [65] both reported significant loss in ductility after gaseous hydrogen charging, while Soundararajan *et al.* [32] reported relatively high resistance to HE after electrochemical hydrogen charging of the same alloy. For the gas-charged samples, the average bulk H concentrations were measured to be around 3200 appm and 1600 appm respectively, at which the samples were clearly embrittled. While the average H concentration in the electrochemically-charged samples was estimated to be around 2400–3000 appm, electrochemical charging induces a steep H concentration gradient near (within tens of microns) to the surface [76, 77], leading to brittle fracture within this surface region while the interior of the sample, which has a much reduced H concentration, exhibited ductile fracture. In general, these results agree with the predictions from our model for cracks propagating in bulk CrCoNi.

Insight into the effect of twins on the HE of CrCoNi may also be inferred from the above-

mentioned experiments. While all samples contained twins, increased nanotwinning was observed in those samples which exhibited better HE resistance. Soundararajan *et al.* observed a higher density of nanotwins in their hydrogen-charged samples compared to uncharged samples, leading them to conclude that hydrogen-promoted mechanical nanotwinning helps strengthen the material and partially offsets the weakening effect of hydrogen-induced intergranular cracking. Yi *et al.* reported that twinning was absent in the CoCrNi alloy, but was observed in a Mo-doped alloy $(CoCrNi)_{97}Mo_3$ which exhibited better HE resistance. They proposed that the twinning-dominated deformation process activated in the Mo-doped alloy reduces the transport of hydrogen to grain boundaries compared to the dislocation-dominated deformation process in CrCoNi. Hence, while the exact mechanism(s) are still unclear, it appears that the presence of high density of nanotwins in a sample may contribute to improved HE resistance.

In addition to CrCoNi, there have also been a few studies which suggest that the interplay between H and nanotwins in related CCAs CoCrFeMnNi and CoNiV may enhance their HE resistance as well [34, 35, 37]. They proposed that H promotes the formation of dense nanotwins which improves the strain hardening, impedes crack propagation, and contributes to the improved HE resistance in these alloys.

The insights from our modeling work do suggest that twin boundaries in CrCoNi are not detrimental – and may even be beneficial – towards HE resistance, since (1) there is no inherently "brittle" direction for crack propagation along a twin boundary, (2) H does not tend to segregate at twin boundaries, and (3) twin boundaries could act as a barrier to an approaching crack. In the context of the HE mechanism considered in this work, we demonstrate that these factors could contribute towards improved HE resistance in twinned samples, similar to that observed in the above studies. However, there are possibly other HE mechanisms at play which we have not considered in this work which may also contribute towards the improved HE resistance.

Finally, we discuss the sensitivity of our model to some of the input parameters. Spatial variation in the material properties (e.g., γ_{USF}, γ_{surf}, γ_{TB}) in random alloys lead to the "band" of predicted K_{Ic} and K_{Ie} values and hence the "windows" of overlap with K_I^{app} instead of a precise intersection. This represents the uncertainty as to which mechanism will be more energetically favorable at any given local region of the material.

Another consequence of the heterogeneity of chemical environments in random alloys is the

distribution of H solution energies. As shown in Figure 3, the H solution energies appear to roughly follow a Gaussian distribution with mean $\bar{E}$ and standard deviation σ. Under similar external conditions (μ, T), and assuming all other material properties (including $\bar{E}$) unchanged, a system with a narrow distribution of H solution energies is predicted to embrittle at much lower H concentrations than a system with a wider distribution of H solution energies (c.f. Table 2). In other words, a system with a wider distribution of H solution energies can accommodate a higher H concentration in the bulk, reducing the driving force for H segregation at crack tips or other defects which promotes embrittlement. Hence, this property, which reflects the diversity of chemical environments in the material, could potentially be used to tailor the HE resistance of random alloys.

$\sigma(E^{\text{sol}})$ (meV)	critical c_{bulk} (appm)
5	400 (120-700)
25	600 (200-1100)
45	1500 (500-3000)
60	2800 (700-7150)
70	3920 (880-10400)

Table 2: The effect of increasing the standard deviation of the H solution energy distribution $\sigma(E^{\text{sol}})$ on the model predictions. Both the average critical H bulk concentration and its associated uncertainty range (indicated in parentheses) increase with increasing $\sigma(E^{\text{sol}})$.

V_m (Å^3)	critical c_{bulk} (appm)
2.7	1850 (600-3850)
2.8	1500 (500-3000)
2.9	1180 (400-2250)

Table 3: The sensitivity of the model predictions to the H interstitial misfit volume V_m.

The model requires inputs of many material properties, most of which we compute directly from first principles in this study. However, some quantities – such as the H misfit volume V_m which appears in Eqn. (5) – are difficult to evaluate accurately from first principles. Misfit volumes of H atoms in metals are typically estimated to be on the order of a few Å^3 [78, 45, 41]; for simplicity, we have chosen a value of $V_m = 2.8$Å^3 following Zhou *et al*. [45] which was shown to give reasonable model predictions in bulk CrCoNi. We estimate that the variation in misfit volumes in our CrCoNi system may be on the order of a few percent or ± 0.1Å^3, based on estimating that the Bader volumes of the octahedral interstitial sites vary by less than ± 4%. The model prediction is somewhat sensitive to the choice of input V_m which is used to estimate the H accumulation at

the crack tip (c.f. Table 3), hence accounting for variation in the misfit volumes in an actual CCA system would lead to even greater uncertainty in the model predictions. However, we believe that the trends predicted by the model, such as the relative susceptibility of bulk vs. twin boundaries to HE, should still be valid.

5. Conclusion

In this work, we have employed a DFT-informed Griffith-Rice model to predict the ductile or brittle response of a crack tip interacting with twin boundaries in CrCoNi CCA and Ni, both in the absence of and presence of hydrogen, and validated our model predictions with MD simulations where possible. This work builds upon the approach demonstrated by Zhou, Tehranchi and Curtin, and extends it by considering the interaction of the crack tip with a twin boundary, which are prevalent in CCAs such as CrCoNi which show improved HE tolerance. By comparing the onset of the ductile-to-brittle transition in crack tip response in different configurations, both our model and MD simulations predict that TBs in fcc metals in general are not inherently more susceptible to HE than the bulk matrix, and could even potentially improve HE resistance as it impedes advancement of an approaching crack while promoting dislocation emission along the TB. While the spatial variation in material properties adds some uncertainty to the prediction of the crack tip behavior in fcc CCAs such as CrCoNi, the same general mechanisms and trends apply, and could be one factor to explain improved HE resistance observed in highly twinned CCA samples. In fact, the impact of TBs in improving HE tolerance in CCAs could be even more strongly felt in CCAs which have high twinnability and which can be engineered to have high nanotwin density or gradient nanotwinned structures.

Acknowledgments

A.M.Z.T., Y.Z. and U.R. were supported by the Agency for Science, Technology and Research (A*STAR) through the Structural Metals and Alloys Program (Grant No. A18B1b0061). Z.L. and H.G. were supported by a research startup grant from Nanyang Technological University (Grant No. 002479-00001) and by the Advanced Models for Additive Manufacturing (AM^2) program under A*STAR (Grant No. M22L2b0111). The computational work for this article was partially performed on resources of the National Supercomputing Centre (NSCC), Singapore

(https://www.nscc.sg), as well as the supercomputer Fugaku provided by the RIKEN Center for Computational Science (Project hp220157).

References

[1] J. R. Rice, Dislocation nucleation from a crack tip: An analysis based on the peierls concept, J. Mech. Phys. Solids 40 (1992) 239–271. doi:10.1016/S0022-5096(05)80012-2.

[2] W. H. Johnson, On some remarkable changes produced in iron and steel by the action of hydrogen and acids, Nature 11 (1875) 393–393. doi:10.1038/011393a0.

[3] J. A. Lee, Gaseous Hydrogen Embrittlement of Materials in Energy Technologies, Elsevier, 2012. doi:10.1533/9780857093899.3.624.

[4] M. Rezende, L. Araujo, S. Gabriel, D. dos Santos, L. de Almeida, Hydrogen embrittlement in nickel-based superalloy 718: Relationship between $\gamma' + \gamma$" precipitation and the fracture mode, Int. J. Hydrog. 40 (2015) 17075–17083. doi:10.1016/j.ijhydene.2015.07.053.

[5] Z. Tarzimoghadam, D. Ponge, J. Klöwer, D. Raabe, Hydrogen-assisted failure in ni-based superalloy 718 studied under in situ hydrogen charging: The role of localized deformation in crack propagation, Acta Mater. 128 (2017) 365–374. doi:10.1016/j.actamat.2017.02.059.

[6] P. Cotterill, The hydrogen embrittlement of metals, Prog. Mater. Sci. 9 (1961) 205–301. doi:10.1016/0079-6425(61)90005-6.

[7] H. C. Rogers, Hydrogen embrittlement of metals, Science 159 (1968) 1057–1064. doi:10.1126/science.159.3819.1057.

[8] C. D. Beachem, A new model for hydrogen-assisted cracking (hydrogen "embrittlement"), Metall. Trans. 3 (1972) 441–455. doi:10.1007/BF02642048.

[9] H. Birnbaum, P. Sofronis, Hydrogen-enhanced localized plasticity—a mechanism for hydrogen-related fracture, Mater. Sci. Eng. A 176 (1994) 191–202. doi:10.1016/0921-5093(94)90975-X.

[10] I. Robertson, The effect of hydrogen on dislocation dynamics, Eng. Fract. Mech. 68 (2001) 671–692. doi:10.1016/S0013-7944(01)00011-X.

[11] M. L. Martin, M. Dadfarnia, A. Nagao, S. Wang, P. Sofronis, Enumeration of the hydrogen-enhanced localized plasticity mechanism for hydrogen embrittlement in structural materials, Acta Mater. 165 (2019) 734–750. doi:10.1016/j.actamat.2018.12.014.

[12] R. Oriani, A mechanistic theory of hydrogen embrittlement of steels, Ber. Bunsenges. Phys. Chem. 76 (1972) 848–857.

[13] R. Kirchheim, Reducing grain boundary, dislocation line and vacancy formation energies by solute segregation. i. theoretical background, Acta Mater. 55 (2007) 5129–5138. doi:10.1016/j.actamat.2007.05.047.

[14] R. Kirchheim, Reducing grain boundary, dislocation line and vacancy formation energies by solute segregation: Ii. experimental evidence and consequences, Acta Mater. 55 (2007) 5139–5148. doi:10.1016/j.actamat.2007.05.033.

[15] J. Song, W. A. Curtin, A nanoscale mechanism of hydrogen embrittlement in metals, Acta Mater. 59 (2011) 1557–1569. doi:10.1016/j.actamat.2010.11.019.

[16] J. Song, W. A. Curtin, Atomic mechanism and prediction of hydrogen embrittlement in iron, Nat. Mater. 12 (2013) 145–151. doi:10.1038/nmat3479.

[17] R. A. Oriani, Whitney award lecture—1987: Hydrogen—the versatile embrittler, Corrosion 43 (1987) 390–397. doi:10.5006/1.3583875.

[18] P. Gong, J. Nutter, P. E. J. Rivera-Diaz-Del-Castillo, W. M. Rainforth, Hydrogen embrittlement through the formation of low-energy dislocation nanostructures in nanoprecipitation-strengthened steels, Sci. Adv. 6 (11 2020). doi:10.1126/sciadv.abb6152.

[19] I. M. Robertson, P. Sofronis, A. Nagao, M. L. Martin, S. Wang, D. W. Gross, K. E. Nygren, Hydrogen embrittlement understood, Metall. Mater. Trans. B 46 (2015) 1085–1103. doi:10.1007/s11663-015-0325-y.

[20] X. Li, X. Ma, J. Zhang, E. Akiyama, Y. Wang, X. Song, Review of hydrogen embrittlement in metals: Hydrogen diffusion, hydrogen characterization, hydrogen embrittlement mechanism

and prevention, Acta Metall. Sin. (Engl. Lett.) 33 (2020) 759–773. doi:10.1007/s40195-020-01039-7.

[21] S. Liang, M. Huang, L. Zhao, Y. Zhu, Z. Li, Effect of multiple hydrogen embrittlement mechanisms on crack propagation behavior of fcc metals: Competition vs. synergy, Int. J. Plast. 143 (2021) 103023. doi:10.1016/j.ijplas.2021.103023.

[22] M. B. Djukic, G. M. Bakic, V. S. Zeravcic, A. Sedmak, B. Rajicic, The synergistic action and interplay of hydrogen embrittlement mechanisms in steels and iron: Localized plasticity and decohesion, Eng. Fract. Mech. 216 (2019) 106528. doi:10.1016/j.engfracmech.2019.106528.

[23] M.-H. Tsai, J.-W. Yeh, High-entropy alloys: A critical review, Mater. Res. Lett. 2 (2014) 107–123. doi:10.1080/21663831.2014.912690.

[24] D. B. Miracle, O. N. Senkov, A critical review of high entropy alloys and related concepts, Acta Mater. 122 (2017) 448–511. doi:10.1016/j.actamat.2016.08.081.

[25] E. P. George, W. A. Curtin, C. C. Tasan, High entropy alloys: A focused review of mechanical properties and deformation mechanisms, Acta Mater. 188 (2020) 435–474. doi:10.1016/j.actamat.2019.12.015.

[26] B. Gludovatz, A. Hohenwarter, D. Catoor, E. H. Chang, E. P. George, R. O. Ritchie, A fracture-resistant high-entropy alloy for cryogenic applications, Science 345 (2014) 1153–1158. doi:10.1126/science.1254581.

[27] B. Gludovatz, A. Hohenwarter, K. V. S. Thurston, H. Bei, Z. Wu, E. P. George, R. O. Ritchie, Exceptional damage-tolerance of a medium-entropy alloy crconi at cryogenic temperatures, Nat. Comm. 7 (2016) 10602. doi:10.1038/ncomms10602.

[28] S. F. Liu, Y. Wu, H. T. Wang, J. Y. He, J. B. Liu, C. X. Chen, X. J. Liu, H. Wang, Z. P. Lu, Stacking fault energy of face-centered-cubic high entropy alloys, Intermetallics 93 (2018) 269–273. doi:10.1016/j.intermet.2017.10.004.

[29] G. Laplanche, A. Kostka, C. Reinhart, J. Hunfeld, G. E. ans E. P. George, Reasons for the superior mechanical properties of medium-entropy crconi compared to high-entropy crmnfeconi, Acta Mater. 128 (2017) 292–303. doi:10.1016/j.actamat.2017.02.036.

[30] B. Cantor, I. Chang, P. Knight, A. Vincent, Microstructural development in equiatomic multicomponent alloys, Mater. Sci. Eng. A 375–377 (2004) 213–218. doi:10.1016/j.msea.2003.10.257.

[31] Z. Zhang, H. Sheng, Z. Wang, B. Gludovatz, Z. Zhang, E. George, Q. Yu, S. Mao, R. Ritchie, Dislocation mechanisms and 3d twin architectures generate exceptional strength-ductility-toughness combination in crconi medium-entropy alloy, Nat. Commun. 8 (2017) 14390. doi:10.1038/ncomms14390.

[32] C. K. Soundararajan, H. Luo, D. Raabe, Z. Li, Hydrogen resistance of a 1 gpa strong equiatomic cocrni medium entropy alloy, Corrosion Science 167 (2020) 108510. doi:10.1016/j.corsci.2020.108510.

[33] J. Yi, X. Zhuang, J. He, M. He, W. Liu, S. Wang, Effect of mo doping on the gaseous hydrogen embrittlement of a cocrni medium-entropy alloy, Corrosion Science 189 (2021) 109628. doi:10.1016/j.corsci.2021.109628.

[34] H. Luo, Z. Li, D. Raabe, Hydrogen enhances strength and ductility of an equiatomic high-entropy alloy, Sci. Rep. 7 (2017) 9892. doi:10.1038/s41598-017-10774-4.

[35] H. Luo, W. Lu, X. Fang, D. Ponge, Z. Li, D. Raabe, Beating hydrogen with its own weapon: Nano-twin gradients enhance embrittlement resistance of a high-entropy alloy, Mater. Today 21 (2018) 1003–1009. doi:10.1016/j.mattod.2018.07.015.

[36] Y. Zhao, D.-H. Lee, M.-Y. Seok, J.-A. Lee, M. P. Phaniraj, J.-Y. Suh, H.-Y. Ha, J.-Y. Kim, U. Ramamurty, J.-I. Jang, Resistance of cocrfemnni high-entropy alloy to gaseous hydrogen embrittlement, Scripta Mater. 135 (2017) 54–58. doi:10.1016/j.scriptamat.2017.03.029.

[37] H. Luo, S. S. Sohn, W. Lu, L. Li, X. Li, C. K. Soundararajan, W. Krieger, Z. Li, D. Raabe, A strong and ductile medium-entropy alloy resists hydrogen embrittlement and corrosion, Nat. Commun. 11 (2020) 3081. doi:10.1038/s41467-020-16791-8.

[38] A. Mohammadi, M. Novelli, M. Arita, J. W. Bae, H. S. Kim, T. Grosdidier, K. Edalati, Gradient-structured high-entropy alloy with improved combination of

strength and hydrogen embrittlement resistance, Corrosion Science 200 (2022) 110253. doi:10.1016/j.corsci.2022.110253.

[39] X. Zhou, W. A. Curtin, First principles study of the effect of hydrogen in austenitic stainless steels and high entropy alloys, Acta Mater. 200 (2020) 932–942. doi:10.1016/j.actamat.2020.09.070.

[40] X.-Y. Zhou, J.-H. Zhu, Y. Wu, X.-S. Yang, T. Lookman, H.-H. Wu, Machine learning assisted design of feconicrmn high-entropy alloys with ultra-low hydrogen diffusion coefficients, Acta Mater. 224 (2022) 117535. doi:10.1016/j.actamat.2021.117535.

[41] X. L. Ren, P. H. Shi, B. D. Yao, L. Wu, X. Y. Wu, Y. X. Wang, Hydrogen solution in high-entropy alloys, Phys. Chem. Chem. Phys. 23 (2021) 27185–27194. doi:10.1039/D1CP04151G.

[42] Z. Xie, Y. Wang, C. Lu, L. Dai, Sluggish hydrogen diffusion and hydrogen decreasing stacking fault energy in a high-entropy alloy, Mater. Today Commun. 26 (2021) 101902. doi:10.1016/j.mtcomm.2020.101902.

[43] X. Li, J. Yin, J. Zhang, Y. Wang, X. Song, Y. Zhang, X. Ren, Hydrogen embrittlement and failure mechanisms of multi-principalelement alloys: A review, J. Mater. Sci. Technol. 122 (2022) 20–32. doi:10.1016/j.jmst.2022.01.008.

[44] D.-H. Lee, Y. H. An, Y. Zhao, J. H. Lee, H. Y. Kim, Y. S. Kim, S. Y. Lee, A novel methodology to estimate hydrogen diffusivity and its applications in revealing hydrogen effects in cocrni medium-entropy alloy versus 316l stainless steel, Int. J. Plast. 169 (2023) 103737. doi:10.1016/j.ijplas.2023.103737.

[45] X. Zhou, A. Tehranchi, W. A. Curtin, Mechanism and prediction of hydrogen embrittlement in fcc stainless steels and high entropy alloys, Phys. Rev. Lett. 127 (2021) 175501. doi:10.1103/PhysRevLett.127.175501.

[46] Y. Cheng, Z.-H. Jin, Y. W. Zhang, H. Gao, On intrinsic brittleness and ductility of intergranular fracture along symmetrical tilt grain boundaries in copper, Acta Mater. 58 (2010) 2293–2299. doi:10.1016/j.actamat.2009.11.033.

[47] J. Moon, O. Bouaziz, H. S. Kim, Y. Estrin, Twinning engineering of a cocrfemnni high-entropy alloy, Scripta Mater. 197 (2021) 113808. doi:10.1016/j.scriptamat.2021.113808.

[48] M. N. Hasan, Y. F. Liu, X. H. An, J. Gu, M. Song, Y. Cao, Y. S. Li, Y. T. Zhu, X. Z. Liao, Simultaneously enhancing strength and ductility of a high-entropy alloy via gradient hierarchical microstructures, Int. J. Plast. 123 (2019) 178–196. doi:10.1016/j.ijplas.2019.07.017.

[49] G. Kresse, J. Hafner, Ab initio molecular dynamics for liquid metals, Phys. Rev. B 47 (1) (1993) 558(R). doi:10.1103/PhysRevB.47.558.

[50] G. Kresse, J. Furthmüller, Efficient iterative schemes for ab initio total-energy calculations using a plane-wave basis set, Phys. Rev. B 54 (16) (1996) 11169—11186. doi:10.1103/PhysRevB.54.11169.

[51] G. Kresse, J. Furthmüller, Efficiency of ab-initio total energy calculations for metals and semiconductors using a plane-wave basis set, Comp. Mater. Sci. 6 (1) (1996) 15–50. doi:10.1016/0927-0256(96)00008-0.

[52] P. E. Blöchl, Projector augmented-wave method, Phys. Rev. B 50 (1994) 17953. doi:10.1103/PhysRevB.50.17953.

[53] G. Kresse, D. Joubert, From ultrasoft pseudopotentials to the projector augmented-wave method, Phys. Rev. B 59 (1999) 1758. doi:10.1103/PhysRevB.59.1758.

[54] J. P. Perdew, K. Burke, M. Ernzerhof, Generalized gradient approximation made simple, Phys. Rev. Lett. 77 (1996) 3865–3868. doi:10.1103/PhysRevLett.77.3865.

[55] M. Methfessel, A. T. Paxton, High-precision sampling for brillouin-zone integration in metals, Phys. Rev. B 40 (1989) 3616. doi:10.1103/PhysRevB.40.3616.

[56] H. J. Monkhorst, J. D. Pack, Special points for brillouin-zone integrations, Phys. Rev. B 13 (1976) 5188—-5192. doi:10.1103/PhysRevB.13.5188.

[57] A. van de Walle, P. Tiwary, M. de Jong, D. L. Olmsted, M. Asta, A. Dick, D. Shin, Y. Wang, L.-Q. Chen, Z.-K. Liu, Efficient stochastic generation of special quasirandom structures, Calphad 42 (2013) 13–18. doi:10.1016/j.calphad.2013.06.006.

[58] A. Zunger, S.-H. Wei, L. G. Ferreira, J. E. Bernard, Special quasirandom structures, Phys. Rev. Lett. 65 (1990) 353. doi:10.1103/PhysRevLett.65.353.

[59] A. Kelly, W. R. Tyson, A. H. Cottrell, Ductile and brittle crystals, Phil. Mag. 15 (1967) 567–586. doi:10.1080/14786436708220903.

[60] J. R. Rice, R. Thomson, Ductile versus brittle behaviour of crystals, Phil. Mag. 29 (1974) 73–97. doi:10.1080/14786437408213555.

[61] D. D. Mason, Segregation-induced embrittlement of grain boundaries, Phil. Mag. A 39 (1979) 455–468. doi:10.1080/01418617908239284.

[62] F. Cleri, S. R. Phillpot, D. Wolf, Atomistic simulations of integranular fracture in symmetric-tilt grain boundaries, Interface Science 7 (1999) 45–55. doi:10.1023/A:1008773913030.

[63] A. A. Griffith, The phenomena of rupture and flow in solids, Philos. Trans. Roy. Soc. Lond. A 221 (1921) 163–198. doi:10.1098/rsta.1921.0006.

[64] C. Sun, Z.-H. Jin, Fracture Mechanics, Elsevier, 2012. doi:10.1016/C2009-0-63512-1.

[65] X. H. Chen, X. Q. Zhuang, J. W. Mo, J. Y. He, T. Yang, X. Y. Zhou, W. H. Liu, Enhanced resistance to hydrogen embrittlement in a crconi-based medium-entropy alloy via grain-boundary decoration of boron, Mater. Res. Lett. 10 (4) (2022) 278–286. doi:10.1080/21663831.2022.2033865.

[66] A. M. Z. Tan, Z. Li, H. Gao, Statistical modeling of the effect of chemical inhomogeneity on incipient plasticity in complex concentrated alloys, Phys. Rev. Mater. 7 (2023) 053601. doi:10.1103/PhysRevMaterials.7.053601.

[67] A. P. Thompson, H. M. Aktulga, R. Berger, D. S. Bolintineanu, W. M. Brown, P. S. Crozier, P. J. in 't Veld, A. Kohlmeyer, S. G. Moore, T. D. Nguyen, R. Shan, M. J. Stevens, J. Tranchida, C. Trott, S. J. Plimpton, LAMMPS - a flexible simulation tool for particle-based materials modeling at the atomic, meso, and continuum scales, Comp. Phys. Comm. 271 (2022) 108171. doi:10.1016/j.cpc.2021.108171.

[68] Q.-J. Li, H. Sheng, E. Ma, Strengthening in multi-principal element alloys with local-chemical-order roughened dislocation pathways, Nat. Commun. 10 (2019) 3563. doi:10.1038/s41467-019-11464-7.

[69] A. Tehranchi, W. A. Curtin, Atomistic study of hydrogen embrittlement of grain boundaries in nickel: I. fracture, J. Mech. Phys. Solids 101 (2017) 150–165. doi:10.1016/j.jmps.2017.01.020.

[70] A. F. Bower, Applied mechanics of solids, CRC press, 2009.

[71] L. Pei, C. Lu, X. Zhao, L. Zhang, K. Cheng, G. Michal, K. Tieu, Brittle versus ductile behaviour of nanotwinned copper: a molecular dynamics study, Acta Mater. 89 (2015) 1–13. doi:10.1016/j.actamat.2015.01.054.

[72] H. L. Mai, X.-Y. Cui, D. Scheiber, L. Romaner, S. P. Ringer, An understanding of hydrogen embrittlement in nickel grain boundaries from first principles, Mater. Des. 212 (2021) 110283. doi:10.1016/j.matdes.2021.110283.

[73] S. Huang, D. Chen, J. Song, D. L. McDowell, T. Zhu, Hydrogen embrittlement of grain boundaries in nickel: an atomistic study, npj Comput. Mater. 3 (2017) 28. doi:10.1038/s41524-017-0031-1.

[74] S. Bechtle, M. Kumar, B. Somerday, M. Laune, R. Ritchie, Grain-boundary engineering markedly reduces susceptibility to intergranular hydrogen embrittlement in metallic material, Acta. Mater. 57 (2009) 4148–4157. doi:10.1016/j.actamat.2009.05.012.

[75] M. Seita, J. P. Hanson, S. Gradečak, M. J. Demkowicz, The dual role of coherent twin boundaries in hydrogen embrittlement, Nat. Commun. 6 (2015) 6164. doi:10.1038/ncomms7164.

[76] Y. Zhao, M.-Y. Seok, I.-C. Choi, Y.-H. Lee, S.-J. Park, U. Ramamurty, J.-Y. Suh, J.-I. Jang, The role of hydrogen in hardening/softening steel: Influence of the charging process, Scripta Mater. 107 (2015) 46–49. doi:10.1016/j.scriptamat.2015.05.017.

[77] Y. Zhao, J.-M. Park, D.-H. Lee, E. J. Song, J.-Y. Suh, U. Ramamurty, J.-I. Jang, Influences of hydrogen charging method on the hydrogen distribution and nanomechanical properties

of face-centered cubic high-entropy alloy: A comparative study, Scripta Mater. 168 (2019) 76–80. doi:10.1016/j.scriptamat.2019.04.025.

[78] X. Zhou, D. Marchand, D. L. McDowell, T. Zhu, J. Song, Chemomechanical origin of hydrogen trapping at grain boundaries in fcc metals, Phys. Rev. Lett. 116 (2016) 075502. doi:10.1103/PhysRevLett.116.075502.